

# Bulk nanomachining of cantilevers with Nb nanoSQUIDs based on nanobridge Josephson junctions

M I Faley<sup>1</sup> , T I Bikulov<sup>2,3</sup>, V Bosboom<sup>4</sup>, A A Golubov<sup>4,5</sup>  and R E Dunin-Borkowski<sup>1,6</sup> 

<sup>1</sup> Peter Grünberg Institute 5, Forschungszentrum Jülich GmbH, 52425 Jülich, Germany

<sup>2</sup> Faculty of Electrical Engineering and Information Technology, RWTH Aachen University, Aachen 52062, Germany

<sup>3</sup> Faculty of Biomedical Engineering, Bauman Moscow State Technical University, 105005 Moscow, Russia

<sup>4</sup> Faculty of Science and Technology, MESA+ Institute for Nanotechnology, University of Twente, 7500 AE Enschede, The Netherlands

<sup>5</sup> The Moscow Institute of Physics and Technology, 141700 Dolgoprudny, Moscow Region, Russia

<sup>6</sup> Ernst Ruska-Centre for Microscopy and Spectroscopy with Electrons, Forschungszentrum Jülich GmbH, 52425 Jülich, Germany

E-mail: [m.faley@fz-juelich.de](mailto:m.faley@fz-juelich.de)

Received 23 November 2020, revised 18 December 2020

Accepted for publication 11 January 2021

Published 2 February 2021



CrossMark

## Abstract

Nanometer-scale superconducting quantum interference devices (nanoSQUIDs) were fabricated within a distance of  $1\ \mu\text{m}$  from the corners of  $2 \times 2 \times 0.05\ \text{mm}$  Si cantilevers that are intended for use in a scanning nanoSQUID microscope. The nanoSQUIDs contained Josephson junctions (JJs) in the form of Nb-based nanobridges, which had widths down to 10 nm and were patterned using hydrogen silsesquioxane negative resist. Numerical simulations of the superconducting current and the spatial distribution of the order parameter in the nanobridge JJs and the nanoSQUID, as well as the current–phase relationship in the nanobridge JJs, were performed according to Ginzburg–Landau equations on one-dimensional and two-dimensional grids. Bulk micromachining of the Si cantilever was performed using reactive ion etching with  $\text{SF}_6$  gas through masks of nLOF 2020 photoresist from the front side and a quartz shadow mask from the back side of the substrate. An etch rate of  $6\ \mu\text{m}\ \text{min}^{-1}$  for Si was achieved for a power of 300 W of the inductively coupled  $\text{SF}_6$  plasma. The nanoSQUIDs exhibited non-hysteretic current–voltage characteristics on the cantilever. The estimated spin sensitivity of  $48\ \mu\text{B}\ (\sqrt{\text{Hz}})^{-1}$  is sufficient for use of such a nanoSQUID as a magnetic field sensor for studying nanoscale objects, with a projected total distance to the object of below 100 nm.

Keywords: bulk nanomachining, nanobridge, Josephson junction, nanoSQUID, cantilever

(Some figures may appear in colour only in the online journal)

## 1. Introduction

Nanometer-scale superconducting quantum interference devices (nanoSQUIDs) are used to perform a wide range of physical measurements (see, e.g. [1] and [2] and references therein). NanoSQUIDs offer the prospect of studying nanoscale magnetic systems with single electron spin sensitivity, memory devices, transition edge sensors for single photon and

macromolecule detection, devices for quantum computing, quantum metrology, etc [1]. In comparison to magnetometers that are based on nitrogen vacancies in diamond, nanoSQUIDs do not need to be illuminated by a laser, which can unintentionally heat a delicate sample operating at low temperature. Furthermore, in contrast to magnetic force microscopy, which uses a magnetized tip that can change the magnetic state of the object, nanoSQUIDs do not contain ferromagnetic parts and

can be used to perform contactless, almost non-destructive measurements because stray magnetic fields from them are much weaker.

NanoSQUIDs have attained an ultra-high electron spin sensitivity of  $<1 \mu_B (\sqrt{\text{Hz}})^{-1}$  [3, 4], an ultra low flux noise of  $\sim 50 n\Phi_0 (\sqrt{\text{Hz}})^{-1}$  [3–5] and an energy resolution approaching the quantum limit [6]. ‘SQUID-on-tip’ nanoSQUIDs have been fabricated by the deposition of Pb or Nb thin films from three directions onto the apices of hollow quartz tubes that were pulled into sharp pipettes with diameters down to  $\sim 39$  nm at their tips [4]. However, such an elegant nanofabrication method has the drawback of a relatively large spread of parameters, restrictions on electrical circuit design and unclear long-term stability of the nanoSQUIDs, limiting their applicability for routine applications. It is more practical to use available planar nanostructuring technologies, in order to achieve greater flexibility in circuit design and passivation and to use bulk nanomachining methods to realize nanoSQUID cantilevers that are compatible with low temperature high-resolution scanning systems.

Nanobridge Josephson junctions (JJs) allow the miniaturization of superconducting devices to a scale that is limited only by the resolution of nanostructuring technologies. Since the Josephson effect was first demonstrated in  $3.6 \mu\text{m}$  wide ‘Dayem’ bridges [7], the spatial resolution of nanostructuring technologies has improved by a factor of  $\sim 1000$ , providing new opportunities for nanoscale patterning (see, e.g. [8, 9]). Progress in nanofabrication has also resulted in a renaissance in the application of nanobridge JJs in superconducting electronics, which was dominated for almost four decades mainly by superconductor-insulator-superconductor (SIS) tunnel JJs based on Nb- $\text{AlO}_x$ -Nb heterostructures [10, 11] or on overdamped JJs, which can be realised in the form of superconductor-normal metal-superconductor or superconductor-insulator-normal metal-insulator-superconductor multilayer structures [12]. Further miniaturization of SIS JJs faces limitations in critical current density  $J_c \cong 50 \text{ kA cm}^{-2}$  that result in a too low critical current  $I_c$  for  $10 \times 10 \text{ nm}$  JJs:  $I_c \cong 50 \text{ nA} \ll I_T \cong 176 \text{ nA}$ , where  $I_T$  is the thermal fluctuation current that corresponds to a Josephson energy of  $E_J \sim k_B T$  at an operating temperature of  $T = 4.2 \text{ K}$ . The critical current density of nanobridge JJs is much higher, approaching the depairing current density of  $\sim 30 \text{ MA cm}^{-2}$  for Nb thin films.

Planar techniques based on electron beam lithography can be used to pattern Nb films with  $10 \text{ nm}$  spatial resolution [13], which is on the order of the coherence length for Nb thin films [14]. Long-term stability of planar nanoSQUIDs can then be realized by depositing a passivation layer and preventing mechanical damage to the nanoSQUID by avoiding direct contact with the object under study. The fabrication of SQUID loops that are thicker than the nanobridges leads to an increased flux modulation depth and much better spin sensitivity [15].

Here, we use electron beam lithography and highly selective reactive ion etching (RIE) to manufacture nanoSQUIDs that have submicrometer lateral dimensions on a Si cantilever chip. Our approach involves the fabrication of nanoSQUIDs

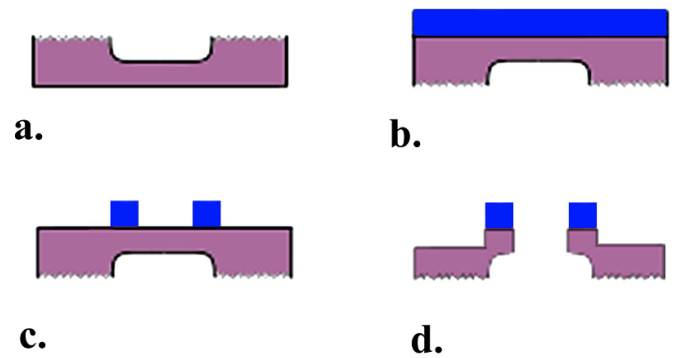


**Figure 1.** Schematic diagrams showing the fabrication process for the nanoSQUID cantilevers: (a) thinning of substrate; (b) deposition of Nb film; (c) structuring of nanoSQUIDs; (d) preparation of suspended cantilevers.

with nanobridge JJs and bulk nanomachining of Si cantilevers, in order to make robust sensors with a customizable layout. The goal is to place a planar nanoSQUID within  $1 \mu\text{m}$  of the corner of a self-made Si cantilever, in order to be able to approach it to an object at a pitch angle of  $<5^\circ$  and at a distance of less than  $100 \text{ nm}$  from it. The corner of the cantilever will then be closer to the object than the nanoSQUID, even at smaller pitch angles, preventing the nanoSQUID from suffering mechanical damage.

## 2. Experimental details and results

### 2.1. Deep etching of Si substrates for the preparation of nanoSQUID cantilevers

NanoSQUID cantilevers were prepared on  $10 \times 10 \times 0.39 \text{ mm}$  Si (001) substrates covered by  $10 \text{ nm}$  thick layers of  $\text{SiO}_2$ . The fabrication steps for the nanoSQUID cantilevers are shown schematically in figure 1. The edges of the substrates were oriented along (100) and (010) crystal planes of Si. The substrates were cleaned in an ultrasonic bath successively in acetone, propanol and double-distilled deionized (DI) water and dried by blowing with  $\text{N}_2$ , before installation in the chamber of a RIE machine (Plasmalab System 100 Oxford Instruments) in the clean room of the Helmholtz Nano Facility (HNF) Forschungszentrum Jülich [16].

By using a  $300 \text{ W}$  inductively coupled plasma (ICP) in pure  $\text{SF}_6$  gas and quartz shadow masks, the  $6 \times 6 \text{ mm}$  area in the middle of the back side of each Si substrate was etched for  $1 \text{ h}$  until a residual thickness of the Si substrate of  $\sim 60 \mu\text{m}$  was attained in this area (figures 1(a) and 2). The edges of the substrates were covered by a bulk quartz shadow mask, so that the edges and front sides of the substrates were protected from etching and remained pristine.

Part of a cross-section of a Si substrate after RIE is shown in the form of a scanning electron microscope (SEM) image in figure 2. Taking into account the much slower etch rate of  $\text{SiO}_2$ , the achieved etch rate of pure Si under these conditions is  $\sim 6 \mu\text{m min}^{-1}$ .

As an alternative to the quartz shadow masks, we tested masks that had been patterned lithographically from up to

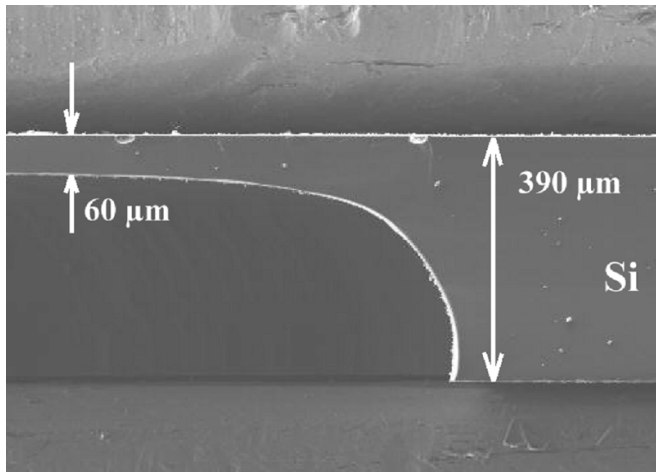


**Figure 2.** SEM image of a cross-section of a Si substrate after 1 h of RIE in  $\text{SF}_6$  gas at a power of 300 W of the ICP.

300  $\mu\text{m}$ -thick negative SU-8 resist. We coated substrates with SU-8 2010 resist without using a spin coater and achieved a flat coverage with a typical thickness of 200  $\mu\text{m}$  in the middle of the substrates, without any edge beads. Structuring of the SU-8 resist was performed with a 1 min exposure using a Mega-UK UV-exposure unit. RIE with 300 W ICP was used for deep etching of the Si substrates and resulted in the same etch rate, but in degradation of the edges of the substrates. Therefore, for most of the samples thinning of the middle parts of the substrates was performed using the quartz shadow masks.

## 2.2. Deposition and characterization of Nb thin films

A base vacuum pressure in the one head sputtering machine of  $5 \times 10^{-8}$  mbar was achieved by using Agilent oil-free turbo and scroll-vacuum pumps. Deposition of Nb films onto the thinned substrates (figure 1(b)) was performed at room temperature using pulsed DC magnetron sputtering in a laminar flow of pure (99.9999%) Ar at  $\sim 8 \times 10^{-3}$  mbar. Superconducting transition temperatures  $T_c$  of between 4.4 and 9.2 K were measured for different thicknesses of Nb films using a Quantum Design Physical Property Measurement System (PPMS) [17]. Fifteen nanometers thick Nb films were measured to have  $T_c \cong 6.4$  K (see figure 3), which is lower than for Nb films deposited on ion-beam-cleaned substrates by electron beam evaporation [18]. The central area in the four-point measurement configuration has a width/length ratio of 2. Reducing the thickness of the Nb film resulted in a broader superconducting transition and a reduction in  $T_c$ . Without passivation, the ultrathin Nb films degraded when they were stored under ambient conditions in the laboratory [18].

A 1 nm thick layer of Ti was deposited onto the Nb film to promote the adhesion of hydrogen silsesquioxane (HSQ) electron beam resist due to the formation of Ti–O bonds between the reactive Ti and the available O atoms in the HSQ resist [19]. The possibility that Ti–Si bonds also form at the interface between Ti and HSQ as a result of electron beam exposure is also advantageous for resist adhesion.

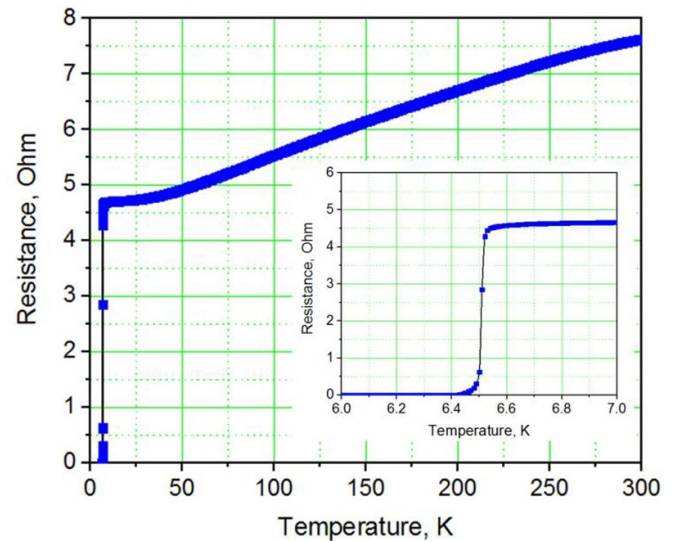


**Figure 3.** Temperature dependence of the resistance  $R(T)$  obtained for a 15 nm thick Nb film. The resistivity of the film is  $\sim 9$  Ohm cm at 10 K.

## 2.3. Preparation of Nb nanoSQUIDs

The samples were spin coated with  $\sim 20$  nm of 2% HSQ electron beam resist immediately after deposition of the adhesion-promoting Ti layer and baked for 2 min at 80  $^{\circ}\text{C}$ . The HSQ resist was exposed to a focused electron beam using an accelerating voltage of 100 kV, a current of 10 nA and a dose of 2.5  $\text{mC cm}^{-2}$ . A post-exposure bake was performed for 2 min at 120  $^{\circ}\text{C}$ . The resist was developed in 25% TMAH for 1 min in an ultrasonic bath, before rinsing the sample in DI water in an ultrasonic bath for 1.5 min, following by rinsing in flowing DI water for 1 min. Contact pads were made from 20 nm thick Pt films that were deposited using DC magnetron sputtering through a Ti shadow mask over the HSQ lines, leading to the nanoSQUID structure.

The Nb films, including the adhesion-promoting Ti film, were patterned (figure 1(c)) using RIE in the clean room of the HNF [16] using pure  $\text{SF}_6$  gas with 25 W of RF plasma without ICP, providing a high selectivity of approximately 10 for etching the Nb and Ti films compared to the HSQ resist. Such a high selectivity of RIE allowed the use of a very thin ( $\sim 20$  nm thick) HSQ resist to achieve a resolution for the Nb nanobridges down to  $\sim 10$  nm (see figure 4 and [13]). As the etch rate of Pt under such RIE conditions is negligible, the Pt contact pads protected the underlying Nb film from RIE. During RIE, the samples were placed freely on a quartz plate cooled from the back side with helium.

Contact pads consisting of a 20 nm thick layer of Pt and a 100 nm thick layer of Au were deposited through a Ti shadow mask. The nanoSQUIDs were covered by a 250 nm thick Si film, which (a) prevented oxidation of the Nb nanobridges; (b) improved heat removal from the nanobridges during operation of the nanoSQUIDs; (c) protected the nanobridges from burnout due to occasional electrostatic discharges at room temperature [20]. Pieces of In placed on the contact pads before deposition of Si could be easily mechanically bonded using

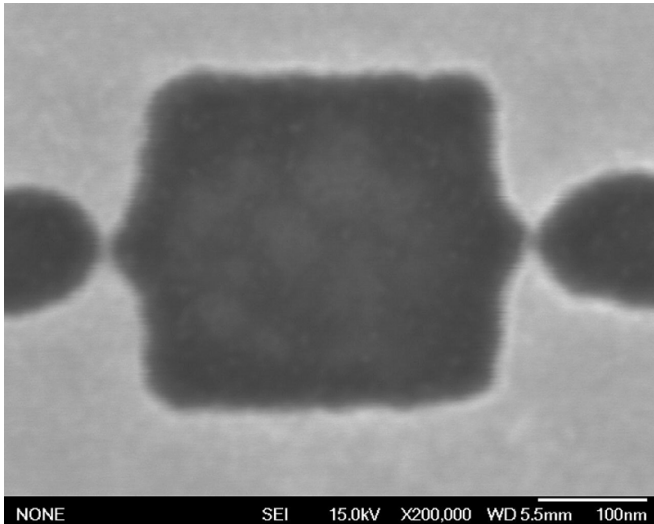


**Figure 4.** SEM image of the loop of the nanoSQUID, with  $\sim 10$  nm wide Nb nanobridge JJs.

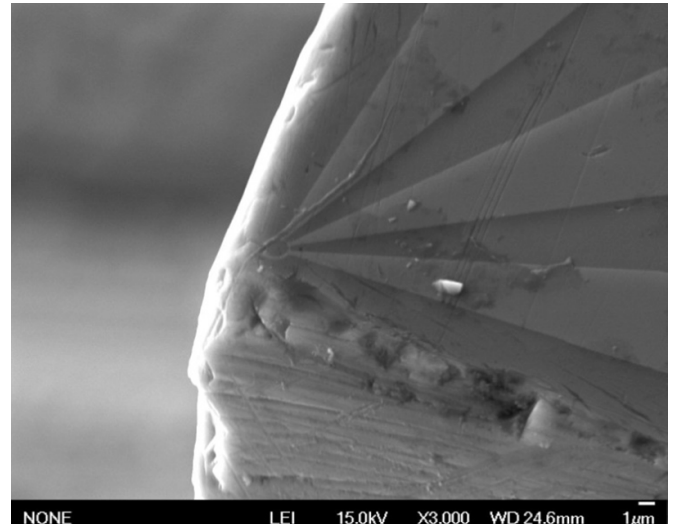


**Figure 5.** SEM image of a nanoSQUID placed within a few micrometers from the corner of a Si cantilever chip using grinding with 4000 grit sandpaper.

Al or Ag wires through the passivating layer of Si, in order to provide galvanic contacts from the nanoSQUIDs to a Quantum Design measurement system or the DC SQUID control electronics.

#### 2.4. Preparation of nanoSQUID cantilever chips

A planar nanoSQUID should be placed onto a cantilever chip that allows for a sufficiently small distance to an investigated object in a scanning system. Micrometer-size SQUIDs (see, e.g. [2, 21, 22]) can be mechanically cut out and formed using a diamond saw and 4000 grit sandpaper with a precision down to about  $\sim 10$   $\mu\text{m}$ , which is limited by the grain size in the sandpaper of  $\sim 6$   $\mu\text{m}$  and by the brittleness of the Si: see [21] and figure 5. The  $\text{SiO}_2$  layer on the surface of the Si substrate increases the roughness of the mechanically-ground corner of the cantilever considerably. The use of finer sandpaper did not help to reduce the roughness of the corner of the cantilever further.

A standard method for bulk micromachining of Si substrates is the deep RIE Bosch process [23]. The Bosch process is relatively slow and results in roughness of  $>10$   $\mu\text{m}$  at an etch rate of  $\sim 55$   $\mu\text{m h}^{-1}$  [22, 24]. RIE in pure  $\text{SF}_6$  gas without the application of ICP has a comparable etch rate.

The nanoSQUIDs were covered by a  $\sim 2$   $\mu\text{m}$  thick negative resist nLOF2020, which was exposed using an electron beam with a dose of  $35$   $\mu\text{C cm}^{-2}$  over the  $2.06 \times 2.06$  mm area of the nanoSQUID and its electrodes, including the contact pads on the cantilever. The distance between the nanoSQUID and the edges of the overlapping photoresist mask was  $30$   $\mu\text{m}$  on each side, in order to compensate for the undercut in the Si substrate during RIE. RIE was performed using pure  $\text{SF}_6$  gas with  $25$  W of radio frequency (RF) plasma without ICP, which provides a high selectivity of more than 13 for deep etching of Si relative to the etch rate of the nLOF2020 resist.

The etch rate for Si in the  $\text{SF}_6$  RF plasma was  $\sim 26$   $\mu\text{m h}^{-1}$  in a direction normal to the substrate surface and  $\sim 16$   $\mu\text{m h}^{-1}$

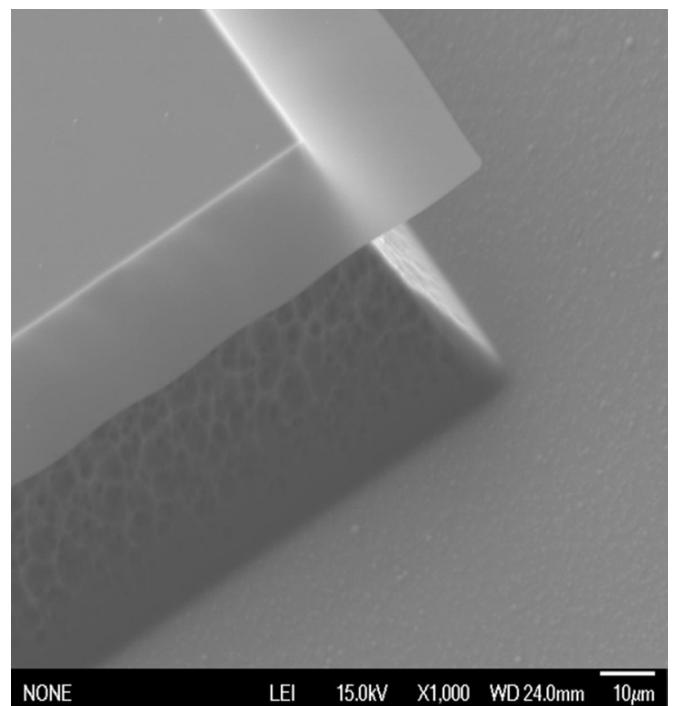


**Figure 6.** SEM image of the corner of the etched area of a Si chip covered by  $10$  nm of  $\text{SiO}_2$  after  $1$  h of RIE in pure  $\text{SF}_6$  gas. The resist is removed by an oxygen plasma.

in the undercut direction. Figure 6 shows an SEM image of the corner of the etched area of a Si chip covered by a  $10$  nm  $\text{SiO}_2$  layer after  $1$  h of RIE in pure  $\text{SF}_6$  gas at  $25$  W RF power. The mask of the nLOF2020 resist was removed by using an oxygen plasma. This process results in a  $10$  nm thick  $\text{SiO}_2$  ‘canopy’ hanging over the undercut area of the etched Si substrate. The corner of the step in the Si substrate has a radius of curvature at the tip of  $<100$  nm and an exactly  $90^\circ$  angle, which would not be possible by etching Si in KOH.

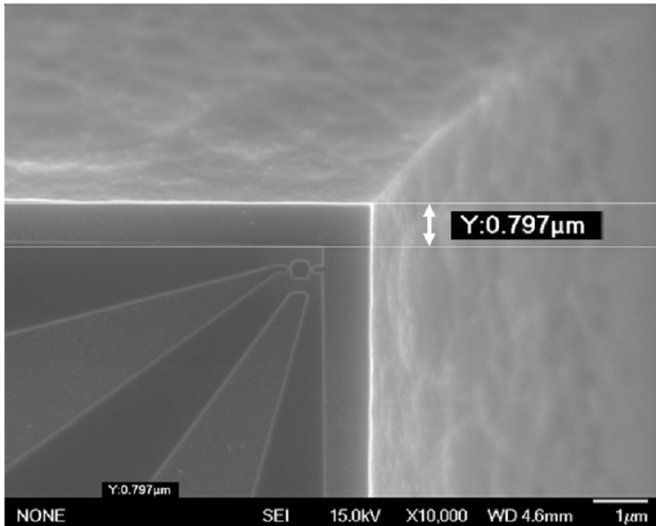


**Figure 7.** SEM image of the corner of a Si chip after  $\sim 1$  h of RIE in pure  $\text{SF}_6$  gas at an RF power of 25 W.

The observed Si etch depends on the etching duration and is reduced significantly if the etching time is less than 15 min. This behavior may be associated with heating of the sample during RIE, with a higher sample temperature leading to a higher etching rate.

RIE was performed in several steps to check the distance between the nanoSQUIDs and the undercut edges by using a Leica INM 100 optical microscope at its highest magnification of  $3000\times$ . After getting the undercut edges close enough to the nanoSQUID, the samples were cleaned in acetone using ultrasonic agitation to partially remove residuals from the resist and the  $\text{SiO}_2$  ‘canopy’, and rinsed in isopropanol and DI water. The rest of the nLOF2020 resist was removed by using an oxygen plasma. The result was a  $\sim 26\text{ }\mu\text{m}$  high step on the Si substrate, with the corner placed within  $\sim 1\text{ }\mu\text{m}$  of the nanoSQUID, as shown in figure 7. The corner of the chip adjacent to the nanoSQUID serving as the cantilever tip has a radius of curvature of  $< 100\text{ nm}$ . The sides are at exactly  $90^\circ$  to each other and parallel to the two extreme electrodes of the nanoSQUID.

The front side of the sample was covered by a  $\sim 10\text{ }\mu\text{m}$  thick photoresist layer and the sample was etched from the back side using RIE at 25 W without ICP until the Si substrate had been etched through in the middle, with the nanoSQUID chip remaining weakly adhered to the Si frame around the substrate perimeter (figure 1(d)). The resist was removed using an oxygen plasma and the individual nanoSQUID chips were cleaved from the frame using fine tweezers or a scalpel blade, as shown in figure 8.

The nanoSQUID chip was glued and bonded to a flexible printed circuit board (PCB) made on  $25\text{ }\mu\text{m}$  thick Kapton foil for further measurements and integration into a scanning system, as shown in figure 9.  $I(V)$  characteristics of the nanoSQUIDs on the cantilever were modulated by using a directly injected or externally applied magnetic field flux.

Figure 10 shows the dependence  $V(B)$  of the voltage  $V$  measured on the nanoSQUID on the externally applied

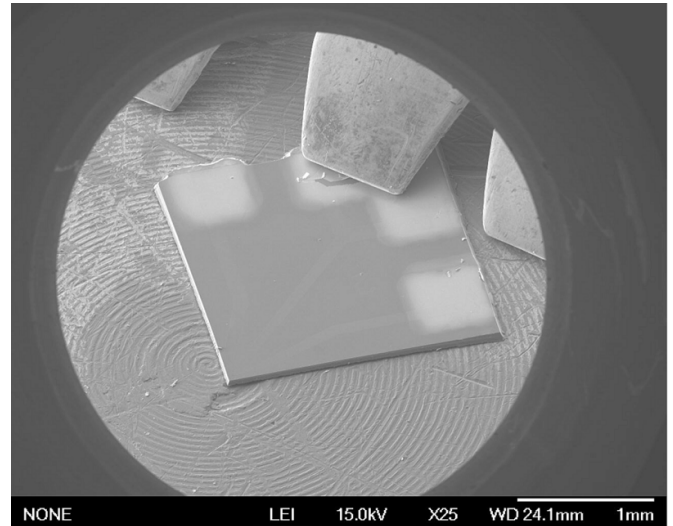


**Figure 8.** SEM image of a  $2 \times 2$  mm Si cantilever chip with contact pads on three corners and a nanoSQUID at the fourth (lower left) corner.

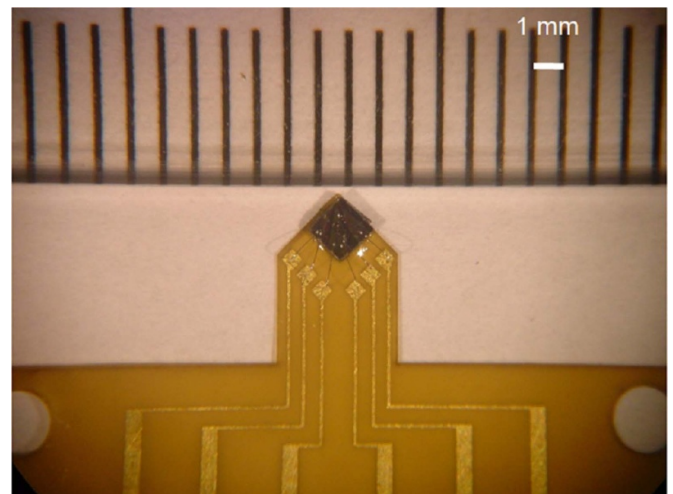


**Figure 9.** SEM image of a nanoSQUID placed on a Kapton PCB.

magnetic field  $B$  recorded using a PPMS. The measurements were performed at the optimal operating temperature for this nanoSQUID of 6 K, at which the current–voltage characteristics are non-hysteretic and the voltage modulation of the nanoSQUID achieves its maximal peak-to-peak value of approximately  $80\text{ }\mu\text{V}$  at a bias current of  $I_B = 31\text{ }\mu\text{A}$ . This temperature can also be maintained in the proposed scanning system, in which the nanoSQUID will be placed in a chamber that is thermally separated from a liquid helium reservoir.

The technology described above can potentially be used for the preparation of electronic circuits, such as superconducting nanostructures on electron-transparent membranes for transmission electron microscopy. By using an offset in position of the photoresist mask, the undercut area can be extended under the electronic circuits, which remain hanging on the ‘canopy’ over the undercut area of the etched Si substrate. An example of a nanoSQUID-on-membrane combination is shown in figure 11.

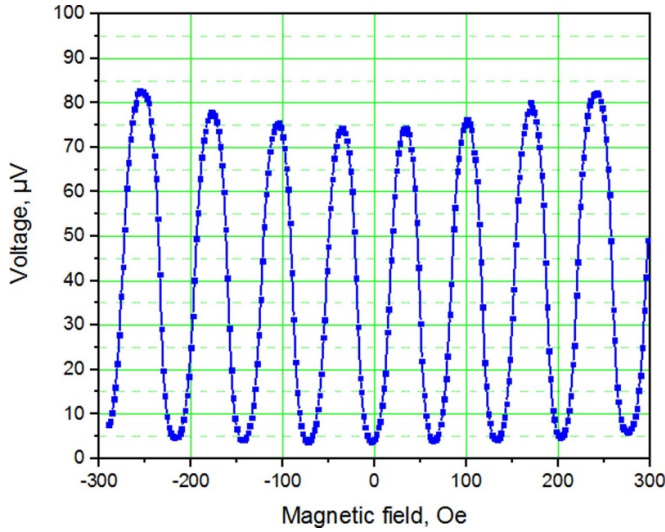


**Figure 10.**  $V(B)$ -dependence of the nanoSQUID made on a  $2 \text{ mm} \times 2 \text{ mm} \times 26 \text{ }\mu\text{m}$  cantilever chip measured at 6 K using a PPMS from Quantum Design.

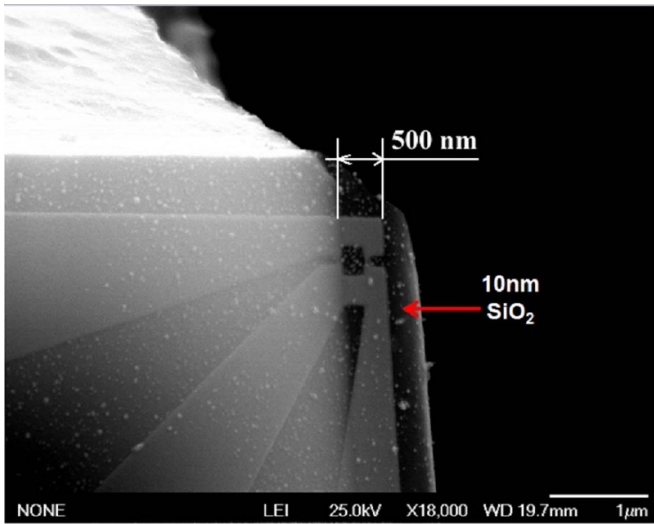


**Figure 11.** SEM image of a nanoSQUID placed within a distance of 500 nm from the corner of a Si cantilever chip on a 10 nm thick  $\text{SiO}_2$  membrane.

The fabrication of JJs in the form of nanobridges allows the production of sufficiently thin active superconducting circuits that do not deteriorate or deform on only 10 nm thick  $\text{SiO}_2$  or SiN membranes that are transparent to electrons. The low energy dissipation in the superconducting circuits provides an additional advantage for their operation on a thin membrane in the ultra high vacuum conditions of an electron microscope.

### 3. Discussion

Bulk nanomachining of a Si chip with Nb nanoSQUIDs placed within  $1 \text{ }\mu\text{m}$  from its corner has been realized without using the SiN hard masks that are typical for bulk micromachining of

Si in Micro-Electro-Mechanical Systems (MEMS) technology [25]. Only a 10 nm-thick native  $\text{SiO}_2$  layer was used as a stop layer for RIE of the Nb film and as a supporting membrane for the nanoSQUID. Neither mechanical polishing nor the Bosch process allowed for the fabrication of nanoSQUID chips with submicrometer precision.

After pre-thinning using high power RIE, the Si substrates still have undamaged frontside surfaces, which are suitable for the deposition of ultra-thin Nb films. A further useful consequence of the high power RIE process is the very gentle slope of the etched area relative to the frontside plane. The middle part of the pre-thinned substrate is then a few micrometers thinner than under the opposite corners of the nanoSQUID chips. This situation allows the nanoSQUID chips to be stored while they are fixed inside the frame of the unetched borders of the  $10 \times 10 \text{ mm}$  substrate and released using a scalpel blade, before installation in a scanning nanoSQUID measurement system.

The nanobridge JJs exhibit a critical current density  $J_c \cong 15 \text{ }\mu\text{A}/(10 \text{ nm})^2 \cong 15 \text{ MA cm}^{-2}$  that is optimal for Nb nanoSQUIDs. The depairing critical current and associated thermal hysteresis loop are observed at  $\sim 2$  times higher bias current. This optimal value of  $J_c$  is much higher than the typical values of critical current density that are measured in high quality SIS tunnel JJs of  $J_c \sim 200 \text{ A cm}^{-2}$  [26] and  $1.7 \text{ kA cm}^{-2}$  [27] in the high quality low- $T_c$  SQUIDs.

#### 3.1. Operating principle of nanobridge JJs

The much higher critical current density in the nanobridge JJs is associated with the different physical nature of the transport of Cooper pairs, as compared to the dominant contribution of tunneling current-transport mechanism in the supercurrent in SIS tunnel JJs (see [28, 29], etc). The Ginzburg–Landau (GL) equation, which is appropriate for nanobridge JJs, can be written in a one-dimensional approximation in the form [29–31]

$$\xi^2 \frac{d^2 f}{dx^2} + f - f^3 = 0, \quad (1)$$

where  $\xi$  is the coherence length and  $f = \Psi/\Psi_\infty$  is the normalized order parameter. In the case of a short length of nanobridge  $L \ll \xi$ , the first term dominates and the equation is reduced to Laplace's equation  $d^2 f/dx^2 = 0$ , for which the solution is the linear function  $f = a + bx$ , with  $x$  ranging from 0 to  $L$ :

$$f = \left(1 - \frac{x}{L}\right) + \left(\frac{x}{L}\right) e^{i\Delta\varphi},$$

where  $\Delta\varphi$  is the phase difference between the wave functions in the electrodes. Insertion of the latter equation for  $f$  into the GL equation for the superconducting current  $I_s$  results in the Josephson current-phase dependence  $I_s = I_c \sin(\Delta\varphi)$ . The influence of quantum fluctuations on the operation of nanoSQUIDs can be neglected due to the high operating temperature of Dayem-type Nb nanobridge JJs, which is usually within  $\sim 10\%$  below  $T_c$  of the used Nb film.

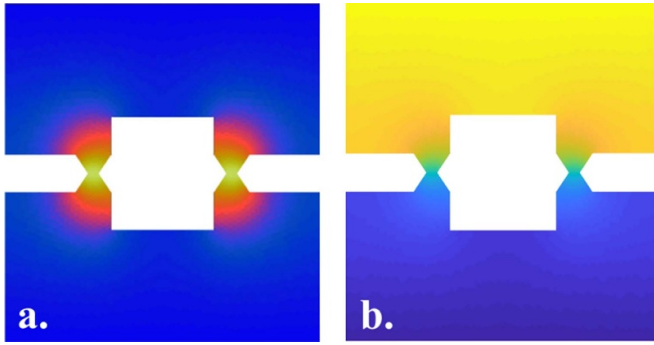


**Figure 12.** Result of a numerical calculation of the 2D distribution of (a) the normalized supercurrent density  $J_s$  and (b) the phase distribution in our nanoSQUID design. The ‘temperature’ color scale is normalized to the difference between the maximal value of  $J_s$  in the middle of the JJs (yellow) and its minimal value in the body of the nanoSQUID (blue). The phase varies according to a color scale from  $0^\circ$  (blue) to  $90^\circ$  (yellow).

For our Dayem-type nanobridges, there is an extra phase gradient in the electrodes that creates a two-dimensional distribution of superconducting current, making the derivation of analytical solutions more complicated. In [32], the two-dimensional GL equation was solved for the case of a hyperbolic bridge with a variable angle.

### 3.2. Numerical simulations of nanobridge JJs

A reduction in temperature of more than  $\sim 10\%$  below  $T_c$  leads to hysteretic current–voltage characteristics that result in a non-sinusoidal multivalued current–phase dependence  $I(\varphi)$  [33]. We performed numerical simulations of current and phase two-dimensional distributions in our nanoSQUID design (figures 12(a) and (b)). The conditions for the multivalued current–phase dependence  $I(\varphi)$  were calculated.

The numerical simulation has shown that in the case of rectangular nanobridge the  $I(\varphi)$ -dependence becomes multivalued at ‘critical’ length  $L_c = 3.49\xi$  corresponding to the one-dimensional critical length [28]. Making a constriction of width  $w$  the middle of nanobridge in the form of bow-tie configuration increases its critical length so that the  $I(\varphi)$ -dependence can remain single-valued also for ratios  $L/\xi > 3.49$  diverging as  $w \rightarrow 0$ .

### 3.3. Analytical approximation and estimate of noise

The  $V(B)$  dependence (see figure 10) of the nanoSQUID at the optimal temperature and bias current can be described to a first approximation by the equation [31]

$$V(\Phi) = \frac{R}{2} \left( I^2 - \left( 2I_c \cos \left( \pi \frac{\Phi}{\Phi_0} \right) \right)^2 \right)^{\frac{1}{2}},$$

with effective area  $A_{\text{eff}} = \Phi/B = 0.36 \mu\text{m}^2$  [13].

The energy sensitivity of the nanoSQUID is limited to a first approximation by Johnson noise, according to the

expression [34]

$$\frac{S}{2L} = \frac{S_V}{(\partial V/\partial \Phi)^2 2L_k} = \frac{16k_B T R_N}{(\partial V/\partial \Phi)^2 2L_k} \cong 57\hbar,$$

where the value  $\partial V/\partial \Phi \cong 220 \mu\text{V}/\Phi_0$  was obtained from figure 10. We obtained an estimated flux sensitivity  $S_\Phi^{1/2} \cong 0.3 \mu\Phi_0 (\sqrt{\text{Hz}})^{-1}$ , a magnetic field resolution  $B_n = (\partial B/\partial \Phi) S_\Phi^{1/2} \cong 2 \text{nT} (\sqrt{\text{Hz}})^{-1}$  and a spin sensitivity  $S_n^{1/2} = S_\Phi^{1/2} r/r_e \cong 48 \mu_B (\sqrt{\text{Hz}})^{-1}$ , where  $r_e = 2.82 \times 10^{-15} \text{m}$  is the classical electron radius [35].

The operation of the nanoSQUID cantilevers in the scanning nanoSQUID measurement system will be described elsewhere.

## 4. Summary

NanoSQUIDs were fabricated within a distance of  $1 \mu\text{m}$  from the corner of a  $2 \times 2 \times 0.05 \text{mm}$  Si cantilever, which is intended for use in a scanning nanoSQUID microscope. The nanoSQUIDs were made with JJs in the form of Nb-based nanobridges, which had widths down to  $10 \text{nm}$  and were patterned using HSQ negative resist. Numerical simulations of the superconducting current, the spatial distribution of the order parameter in the nanobridge JJs and the nanoSQUID, as well as the current–phase relationship in the nanobridge JJs, were performed using GL equations on both one-dimensional and two-dimensional grids. Bulk micromachining of the Si cantilever was performed using RIE with  $\text{SF}_6$  gas through masks of nLOF 2020 photoresist from the front side of the Si substrate and a quartz shadow mask from the back side of the substrate. An etch rate of  $6 \mu\text{m min}^{-1}$  for Si was achieved at a  $300 \text{W}$  power of the inductively coupled  $\text{SF}_6$  plasma. Non-hysteretic current–voltage characteristics were measured for the nanoSQUIDs on a cantilever at  $6 \text{K}$ . The estimated spin sensitivity of  $48 \mu_B (\sqrt{\text{Hz}})^{-1}$  is sufficient for the use of such a nanoSQUID as a magnetic field sensor for the investigation of nanoscale objects, with a projected total distance between the nanoSQUID and an object of  $<100 \text{nm}$ .

## Acknowledgments

This work was supported by the PGI-5 FZJ CEI E-Project ASPIC (E.23102.76). The authors gratefully acknowledge fruitful discussions with V S Stolyarov, H Fiadziushkin and J Liu, the possibility to perform parts of the work at ER-C-1, HNF, PGI-4/JCNS-2, PGI-5 and PGI-7 of the Forschungszentrum Jülich GmbH, as well as technical assistance from H Stumpf, M Nonn, S Trellenkamp, F Lentz, S Nandi, B Schmitz, and R Borowski.

## ORCID iDs

M I Faley <https://orcid.org/0000-0003-2768-2796>

A A Golubov <https://orcid.org/0000-0001-5085-5195>

R E Dunin-Borkowski <https://orcid.org/0000-0001-8082-0647>

## References

- [1] Foley C P and Hilgenkamp H 2009 *Supercond. Sci. Technol.* **22** 064001
- [2] Granata C and Vettoliere A 2016 *Phys. Rep.* **614** 1–69
- [3] Vasyukov D et al 2013 *Nat. Nanotechnol.* **8** 639–44
- [4] Anahory Y et al 2020 *Nanoscale* **12** 3174
- [5] Levenson-Falk E M, Antler N and Siddiqi I 2016 *Supercond. Sci. Technol.* **29** 113003
- [6] Mitchell M W and Alvarez S P 2020 *Rev. Mod. Phys.* **92** 021001
- [7] Anderson P W and Dayem A H 1964 *Phys. Rev. Lett.* **13** 195–7
- [8] Manfrinato V R, Stein A, Zhang L, Nam C-Y, Yager K G, Stach E A and Black C T 2017 *Nano Lett.* **17** 4562–7
- [9] Yang J, Cord B, Duan H, Berggren K, Klingfus J, Nam S, Kim K and Rooks M 2009 *J. Vac. Sci. Technol. B* **27** 2622–7
- [10] Gurvitch M, Washington M A and Huggins H A 1983 *Appl. Phys. Lett.* **42** 472
- [11] Tolpygo S K, Bolkhovsky V, Weir T J, Johnson L M and Gouker M A 2015 *IEEE Trans. Appl. Supercond.* **25** 1–12
- [12] Kohlmann J, Müller F, Kieler O, Behr R, Palafox L, Kahmann M and Niemeyer J 2007 *EEE Trans. Instrum. Meas.* **56** 472–5
- [13] Rodrigo R, Faley M I and Dunin-Borkowski R E 2020 *J. Phys. Conf. Ser.* **1559** 012011
- [14] Draskovic J, Lemberger T R, Peters B, Yang F, Ku J, Bezryadin A and Wang S 2013 *Phys. Rev. B* **88** 134516
- [15] Chen L, Wang H, Liu X, Wu L and Wang Z 2016 *Nano Lett.* **16** 7726–30
- [16] (Available at: [www.fz-juelich.de/hnf/DE/Home/home\\_node.html](http://www.fz-juelich.de/hnf/DE/Home/home_node.html)) (Accessed 21 January 2021)
- [17] (Available at: <https://qd-europe.com/at/en/product/physical-property-measurement-system-ppms/>) (Accessed 21 January 2021)
- [18] Santavica D F and Prober D E 2015 *IEEE Trans. Appl. Supercond.* **25** 2200104
- [19] Macintyre D S, Young I, Glidle A, Cao X, Weaver J M R and Thoms S 2006 *Microelectron. Eng.* **83** 1128–31
- [20] Holdeman L B and Peters P N 1976 *Appl. Phys. Lett.* **28** 632
- [21] Huber M E, Koshnick N C, Bluhm H, Archuleta L J, Azua T, Björnsson P G, Gardner B W, Halloran S T, Lucero E A and Moler K A 2008 *Rev. Sci. Instrum.* **79** 053704
- [22] Hasselbach K, Ladam C, Dolocan V O, Hykel D, Crozes T, Schuster K and Mailly D 2008 *J. Phys. Conf. Ser.* **97** 012330
- [23] Laermer F and Schilp A 2001 Patent US 6,284,148 B1
- [24] Gogolides E, Boukouras C, Kokkoris G, Brani O, Tserepi A and Constantoudis V 2004 *Microelectron. Eng.* **73–74** 312–8
- [25] Gad-El-Hak M (ed) 2006 *MEMS: Design and Fabrication* (Boca Raton, FL: CRC Press Taylor & Francis Group) 647
- [26] Stolz R, Fritzsche L and Meyer H-G 1999 *Supercond. Sci. Technol.* **12** 806–8
- [27] Schmelz M, Stolz R, Zakosarenko V, Anders S, Fritzsche L, Schubert M and Meyer H-G 2011 *Supercond. Sci. Technol.* **24** 015005
- [28] Likharev K K 1979 *Rev. Mod. Phys.* **51** 101
- [29] Aslamazov L G and Larkin A I 1968 *Pis'ma Zh. Eksp. Teor. Fiz.* **9** 150–4
- [30] Schmidt V V 1997 *The Physics of Superconductors* ed P Müller and A V Ustinov (Berlin: Springer) (<https://doi.org/10.1007/978-3-662-03501-6>)
- [31] Tinkham M 1996 *Introduction to Superconductivity* ed Shira J and Castellano E (New York: McGraw-Hill)
- [32] Rogalla H and Heiden C 1989 *Superconducting Quantum Electronics* ed Kose V (Berlin: Springer) pp 80–127
- [33] Troeman A G P, Shw V D P, Il'ichev E, Meyer H-G, Golubov A A, Kupriyanov M Y and Hilgenkamp H 2008 *Phys. Rev. B* **77** 024509
- [34] Tesche C D and Clarke J 1977 *J. Low Temp. Phys.* **29** 301–31
- [35] Ketchen M B, Awschalom D D, Gallagher W J, Kleinsasser A W, Sandstrom R L, Rozen J R and Bumble B 1989 *IEEE Trans. Magn.* **25** 1212–5